Edinburgh Research Explorer

Hybrid Learning based Cell Aggregate Imaging with Miniature Electrical Impedance Tomography

OPEN ACCESS

Hybrid Learning based Cell Aggregate Imaging with Miniature Electrical Impedance Tomography

Zhou Chen, *Student Member, IEEE,* Yunjie Yang, *Member, IEEE*, and Pierre Bagnaninchi

Abstract—Real-time, non-destructive and label-free imaging of 3-D cell culture process using miniature Electrical Impedance Tomography (mEIT) is an emerging topic in tissue engineering. Image reconstruction of mEIT for cell culture is challenging due to weak sensing signals and increased sensitivity to sensor imperfection. Conventional regularization based image reconstruction methods can not always achieve satisfactory performance in terms of image quality and computational efficiency for this particular setup. Recent advances of deep learning have pointed out a promising alternative. However, with a single neural network, it is still difficult to reconstruct multiple objects with varying conductivity levels, which cases are widespread in the application of cell imaging. Aiming at this challenge, in this paper we propose a deep learning and group sparsity regularization based hybrid algorithm for cell imaging with mEIT. A deep neural network is proposed to estimate the structural information in form of binary masks given the limited amount of data sets. Then the structural information is encoded in group sparsity regularization to obtain the final estimation of conductivity. The proposed approach is validated by both simulation and experimental data on MCF-7 human breast cancer cell aggregates, which demonstrates its superior performance and generalization ability compared with a number of existing algorithms.

Index Terms—cell imaging, deep learning, electrical impedance tomography, hybrid learning, image reconstruction

I. INTRODUCTION

RAPID imaging of 3-D cell culture processes [1] in a label-free, non-destructive manner is becoming increasingly attractive in tissue engineering, especially for drug discovery and long-term biological behavior monitoring. Electrical Impedance Tomography (EIT) is a tomographic modality which visualizes the cross-section conductivity distribution by injecting currents and measuring induced voltages at the boundary electrodes of its sensing region [2]. EIT has appealing properties of non-destructiveness, low cost, portability, radiation-free measurement and real-time imaging capability. In the past decades, EIT has been extensively investigated for biomedical imaging, such as functional lung imaging [3], breast cancer detection [4], [5] and brain imaging [6], [7], etc. Recently, EIT has exhibited great potential in the field of tissue engineering. Emerging applications include cell culture imaging [8], [9], cell-drug response imaging [10], cell growth and viability assessment [11], monitoring of single cell mitosis [12], and tissue electroporation imaging [13]. Among these

Z. Chen and Y. Yang are with the Intelligent Sensing, Analysis and Control Group, Institute for Digital Communications, School of Engineering, University of Edinburgh, Edinburgh, UK, EH9 3JL (E-mail: y.yang@ed.ac.uk).

P. Bagnaninchi is with the Centre for Regenerative Medicine, Institute for Regeneration and Repair, University of Edinburgh, Edinburgh EH16 4UU. (e-mail: Pierre.Bagnaninchi@ed.ac.uk).

Manuscript received xx, 2020.

applications, cell imaging with EIT has been particularly challenging in solving the EIT-image-reconstruction problem. The trend of sensor micro-miniaturization in cell imaging [8]–[10] has led to much weaker measurement signals and increased sensitivity to sensor imperfection, which requires to improve spatial resolution and obtain robust, high-quality image reconstruction. In addition, the need to process large amount of sensing data sequences in real-time for cell imaging suggests that high computational efficiency is preferable.

As a typical inverse problem, EIT image reconstruction in essence suffers from nonlinearity, under-determination and ill-posedness. Existing approaches commonly employ regularization to stabilize their solutions. Some prevailing regularization methods include Tikhonov regularization [14], Total Variation (TV) regularization [15], sparsity (or l_1) regularization [16], [17] and its variety [18], etc. Particularly, 3-D TV and l_1 joint regularization was previously proposed by the authors for 3-D cell culture imaging [9]. Recently, novel image reconstruction approaches from statistical perspectives have stimulated new insights to solve this problem. Examples include Structure-Aware Sparse Bayesian Learning (SA-SBL) for 2D EIT image reconstruction [19] and its extended version to deal with 3-D geometries [20]. Whilst time-consuming, results of these methods suggest that introducing structural sparsity information as priori knowledge leads to significant improvement of image quality. Despite the remarkable progress of these state-of-the-art algorithms, further improvements are still in demand in terms of spatial resolution, noise resistance performance and computational efficiency in order to facilitate high-quality cell imaging with the miniature EIT (mEIT) setup.

Data-driven or learning-based methods recently have become a new frontier for tomographic image reconstruction, particularly for mature medical imaging modalities [21]. Although these methods rely heavily on the quality and availability of training data sets and can have a considerable training time, the significant improvement in image quality and fast inference capability contribute to their growing popularity. Existing learning-based image reconstruction algorithms for Computed Tomography (CT), Positron Emission Tomography (PET), Magnetic Resonance Imaging (MRI), and Photoacoustic Tomography [21] can be generally classified as (a) image domain learning, which mainly removes artifacts of post-reconstructed images [22], (b) data domain learning, a more aggressive strategy that directly maps measurement data to images [23], (c) hybrid methods, which uses machine learning to provide image prior [24], and (d) end-to-end workflows, where image reconstruction and analysis are trained jointly [25]. In the field of electrical tomography, Zheng et al. [26]

proposed an auto-encoder structure and Tan et al. [27] developed a LeNet-like network to reconstruct image for electrical tomography. Hu et al. [28] introduced a Convolutional Neural Network (CNN) to map directly the measurement data to conductivity distribution, while further taking into account the geometrical structure of EIT sensors. These methods utilize data domain learning structure and demonstrate the superiority of deep learning methods over conventional image reconstruction methods. However, a significant limitation of these work is that only single-level (or binary) conductivity/permittivity changes are investigated, which is far from the practical scenarios with multi-level conductivity/permittivity distributions.

In this paper, we target to address this more challenging multi-level EIT image reconstruction problem that is frequently encountered in cell imaging. The main contribution of this work lies in the development of a novel Deep Neural Network (DNN) and physical model based hybrid image reconstruction framework for effective recovering of multi-level conductivity distributions. As it is very challenging to estimate continuous, multi-level conductivity changes by using a single neural network with limited training data, we split the problem into two sub-tasks, i.e. DNN based structural information estimation and physical model based conductivity prediction. Some recent work [29], [30] has demonstrated the success of combining DNN with the physical EIT model, where DNNs implement post-processing to remove artefacts of the initial low quality images generated from physical model based reconstruction. Differently, in the proposed framework, we first leverage DNN to predict binary structural information, and then determine the conductivity in a continuous manner using regularization. We establish a DNN named FC-UNet to identify binary structural information, i.e. position and geographical shape of each object within the sensing region. The structural information is then encoded into Group Sparsity (GS) regularization [18], an iterative framework utilizing the structural information as constraint, to further estimate the conductivity levels of each object. The framework is named as DL-GS and we demonstrate its effectiveness and superiority based on phantom simulation and real-world data on MCF-7 breast cancer cell aggregates.

This paper is organized as follows. Section II introduces the principle of EIT and the DL-GS framework. Section III presents the experimental setup. Section IV demonstrates results based on simulation data and cell data. Finally, Section V draws conclusions and discusses future work.

II. METHODOLOGY

A. Principle of EIT

EIT-image-reconstruction problem is to estimate the conductivity distribution within a sensing region by means of injecting currents and measuring the induced boundary voltage differences. In general, EIT measurements could be modeled by the prevailing Complete Electrode Model (CEM) under certain assumptions [31]. The relationship between conductivity distribution, i.e. $\boldsymbol{\sigma} \in \mathbb{R}^n$, and voltage measurements, i.e. $\mathbf{V} \in \mathbb{R}^m$, is in essence non-linear, and can be generally expressed as

$$\mathbf{V} = F(\boldsymbol{\sigma}) \tag{1}$$

In practice, the linearized format of (1) is commonly adopted, which assumes a perturbation of conductivity distribution, i.e. $\Delta\boldsymbol{\sigma} \in \mathbb{R}^n$, and considers its relationship with the change of induced boundary voltages, i.e. $\Delta\mathbf{V} \in \mathbb{R}^m$. The linearized EIT model is given by

$$\Delta\mathbf{V} = \mathbf{J}\Delta\boldsymbol{\sigma} \tag{2}$$

where $\mathbf{J} \in \mathbb{R}^{m \times n}$ donates the Jacobian matrix (also known as the sensitivity matrix). The sensitivity at the kth pixel of the sensing region is calculated by

$$\mathbf{J}_{ij}(k) = \frac{\partial V_{ij}}{\partial \sigma_k} = -\int_{pixel\,k} \nabla\mathbf{u}(I_i) \cdot \nabla\mathbf{u}(I_j)dV \tag{3}$$

where $\nabla\mathbf{u}(I_i)$ and $\nabla\mathbf{u}(I_j)$ are gradients of the potential fields $\mathbf{u}$, when the current is injected into the ith and j^{th} electrode pairs, respectively.

Conventionally, the EIT image reconstruction problem based on (2) can be formulated as the following constrained problem:

$$\begin{cases} \min_{\Delta\boldsymbol{\sigma}} \mathcal{R}(\Delta\boldsymbol{\sigma}) \\ s.t.\,\mathbf{J}\Delta\boldsymbol{\sigma} = \Delta\mathbf{V} \end{cases} \tag{4}$$

where $\mathcal{R}$ denotes the regularization function, which integrates the prior knowledge of $\Delta\boldsymbol{\sigma}$ to avoid outliers in estimation.

B. DL-GS Framework

Fig. 1 presents the schematic illustration of the proposed DL-GS framework, where the input is boundary voltage measurement, and the output is conductivity. We first construct a deep convolutional neural network to estimate the conductivity distribution with input of voltage measurement. This network focuses on distinguishing inclusions from background substances and results are presented in a binary format. To train the network, we establish a training data set with multi-level conductivity distributions by finite element modelling with COMSOL Multiphysics (see details in Section III-A). The binary result is then fed into a group index encoder, which generates a pixel grouping index vector depicting the underlying structural information of the conductivity [18]. As prior knowledge, the structural information is finally integrated into Group Sparsity (GS) regularization to estimate conductivity values in a continuous manner.

1) Network Architecture: The objective of the neural network is to predict the positions and shapes of all possible objects, given the boundary voltage measurement. The neural network consists of a Fully Connected (FC) layer and a UNet [32] (see Fig. 2), therefore it is named as FC-UNet. In our previously reported Adaptive Group Sparsity (AGS) algorithm [18], the estimation of the positions and shapes of objects was achieved by a one-step Gaussian Newton solver with Laplacian regularization [33]. This method is limited in that the results are coarse and sensitive to noise, which poses a challenge to determine the boundary of objects accurately. In contrast,
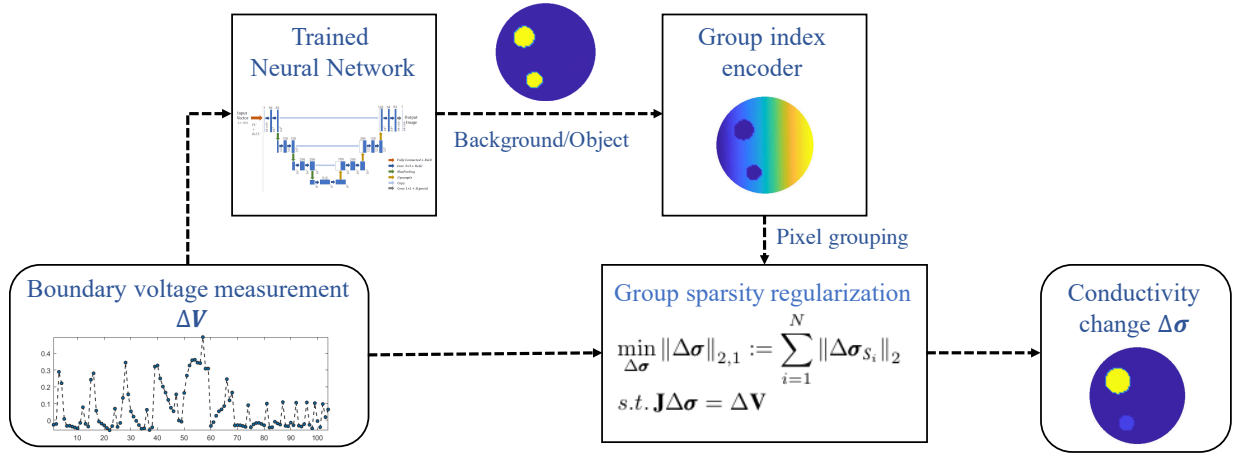
Fig. 1. Schematic illustration of the proposed DL-GS framework.

the proposed FC-UNet is designed to enable faster and more accurate predictions.

As illustrated in Fig. 2, in FC-UNet, we first introduce a FC layer followed by a ReLU layer to implement an inital estimate of the conductivity distribution. A UNet-like architecture, which was proposed especially for biomedical image segmentation [32], is employed afterwards to denoise the output of the FC layer. The main architecture of UNet is a typical auto-encoder, which maps an image to a low-dimension tensor and then reconstructs it back to an image. The contraction on the left hand side comprises a stack of convolutional and max pooling layers. It applies two 3×3 convolutional layers with a 2×2 max pooling in each step whereas the layer at the bottom employs a 2×2 upsample layer after convolutions. The expansion on the right hand side is more or less symmetric to the contraction, using transposed convolutions to facilitate accurate localization. Skip connections are also inserted in expansion to capture tiny details and mitigate the vanishing gradient problem, where the corresponding feature maps from the contraction part are reused and concatenated in expansion steps. The feature maps are appended directly after the upsample layer. Finally, after the two-convolution operation, a 1×1 convolutional layer and a sigmoid layer are used for classification. To choose a UNet structure well suited to EIT image reconstruction problems, we need to reduce hidden layers in the original architecture as a trade-off due to the considerable parameters for the FC layer at the beginning (i.e. 104×4096). After performing hyper-parameter searching on validation data set, we determine to have one less contraction step and one less expansion step.

Each pixel is eventually classified into either background or object. Then the binary mask $\mathbf{M} \in \mathbb{R}^n$ is given by the output, $\mathbf{M} = f_{FC-UNet}(\Delta\mathbf{V}|\boldsymbol{\theta})$, where $f_{FC-UNet}$ is the forward mapping of the FC-UNet parameterised by network weights $\boldsymbol{\theta}$. The network parameters $\boldsymbol{\theta}$ are learned during training. We use binary-cross-entropy as the loss function to train the FC-UNet:

$$\mathcal{L}(\boldsymbol{\theta}) = -\frac{1}{K}\sum_{i=1}^{K}(\mathbf{M}_i \cdot log\hat{\mathbf{M}}_i + (1 - \mathbf{M}_i) \cdot log(1 - \hat{\mathbf{M}}_i)) \quad (5)$$

where $\hat{\mathbf{M}}_i$ denotes the ground truth, and K is the total number

of input-target pairs in the training data set.

2) Group Index Encoder: The group index encoder is to partition all pixels within the sensing region into different groups based on the structural information depicted by the binary mask $\mathbf{M}$ from FC-UNet. Assuming the conductivity change $\Delta\sigma$ can be classified into N groups, i.e.

$$\Delta\boldsymbol{\sigma} = \{\Delta\boldsymbol{\sigma}_{S_1}, \Delta\boldsymbol{\sigma}_{S_2}, \dots, \Delta\boldsymbol{\sigma}_{S_N}\} \quad (6)$$

where $S_i, i = 1, 2, \dots, N$ denotes the group index of the ith group. The strategy of the group index encoder is (see Fig. 3 for schematic illustration):

1) pixel clusters classified as an object will be defined as a large group and assigned the same group index value; different objects correspond to different large groups; (the example in Fig. 3 has two large groups, i.e. $\Delta\boldsymbol{\sigma}_{S_1}, \Delta\boldsymbol{\sigma}_{S_2}$)
2) individual pixels classified as background will be defined as a series of small groups; (Fig. 3 has $\Delta\boldsymbol{\sigma}_{S_3}, \dots, \Delta\boldsymbol{\sigma}_{S_N}$)
3) consecutive integers are assigned as group index for each group, i.e. 1, 2,..., N;
4) the grouping follows $\bigcup_{i=1}^{N} \Delta\boldsymbol{\sigma}_{S_i} = \Delta\boldsymbol{\sigma}$.

3) Group Sparsity Regularization: After obtaining the pixel grouping result, we impose this structural characteristics as a-priori information and estimate the continuous conductivity by using group sparsity regularization [18]. As reported in [18], group sparsity promotes the underlying structural informa-tion of conductivity distribution. The constrained optimization problem can be formulated as

$$\begin{cases} \min_{\Delta\boldsymbol{\sigma}} \|\Delta\boldsymbol{\sigma}\|_{2,1} := \sum_{i=1}^{N} \|\Delta\boldsymbol{\sigma}_{S_i}\|_2 \\ s.t.\, \mathbf{J}\Delta\boldsymbol{\sigma} = \Delta\mathbf{V} \end{cases} \quad (7)$$

where $\|\cdot\|_{2,1}$ denotes the $l_{2,1}$ norm, which is the sum of energy of each defined group. It has been proved to facilitate group sparsity, i.e. minimizing the $l_{2,1}$ norm suppresses pixel groups with very small energies while promoting those present large energies [34], [35]. In this way, it takes advantage of the structural prior and improves image quality.
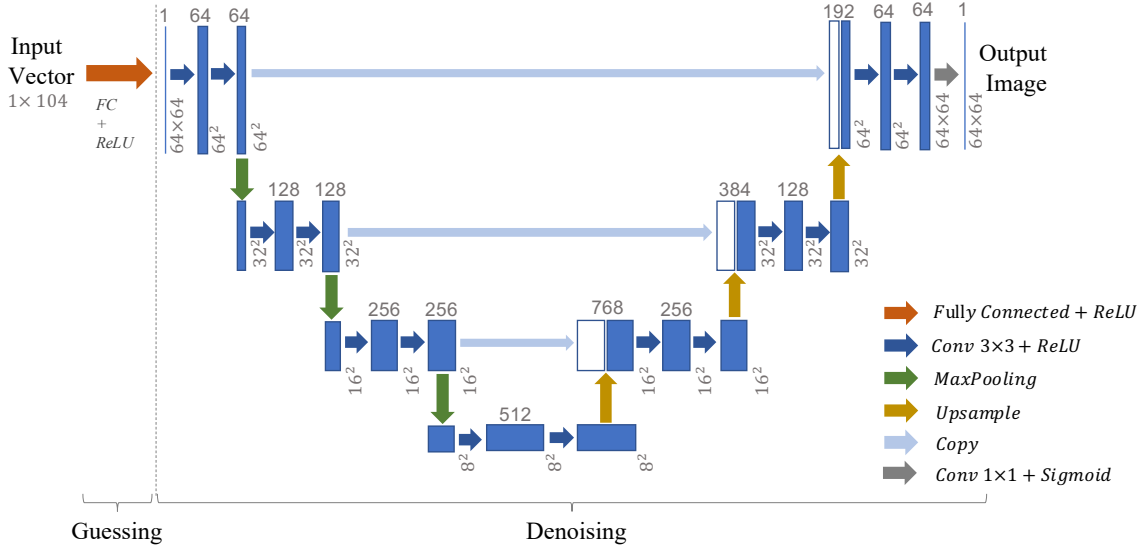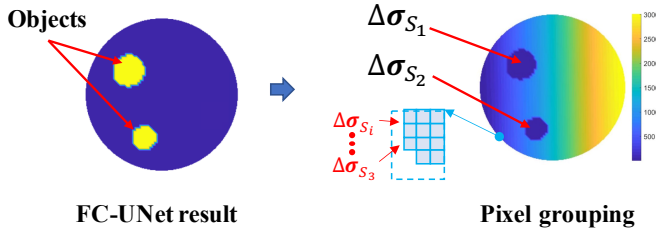
Fig. 2. The architecture of FC-UNet.

Fig. 3. Pixel grouping based on FC-UNet result.

We apply the Alternating Direction Method of Multipliers (ADMM) to solve (7). ADMM is a prevailing approach for solving the constrained separable optimization problems by breaking the objective function into a number of sub-problems without coupled variables [36], [37]. By introducing an auxiliary vector $\mathbf{x} \in \mathbb{R}^n$, the problem in (7) can be rewritten as

$$\begin{cases} \min_{\Delta\boldsymbol{\sigma},\mathbf{x}} \sum_{i=1}^{N} \|\mathbf{x}_{S_i}\|_2 \\ s.t.\, \mathbf{x} = \Delta\boldsymbol{\sigma},\, \mathbf{J}\Delta\boldsymbol{\sigma} = \Delta\mathbf{V} \end{cases} \tag{8}$$

Equivalently, we solve the following augmented Lagrangian problem.

$$\min_{\Delta\boldsymbol{\sigma},\mathbf{x}} \sum_{i=1}^{N} \|\mathbf{x}_{S_i}\|_2 - \boldsymbol{\gamma}_1^{\mathrm{T}}(\mathbf{x} - \Delta\boldsymbol{\sigma}) + \frac{\alpha_1}{2}\|\mathbf{x} - \Delta\boldsymbol{\sigma}\|_2^2 - \\ \boldsymbol{\gamma}_2^{\mathrm{T}}(\mathbf{J}\Delta\boldsymbol{\sigma} - \Delta\mathbf{V}) + \frac{\alpha_2}{2}\|\mathbf{J}\Delta\boldsymbol{\sigma} - \Delta\mathbf{V}\|_2^2 \tag{9}$$

where $\boldsymbol{\gamma_1}, \boldsymbol{\gamma_2} \in \mathbb{R}^n$ are multipliers and $\alpha_1, \alpha_2 \in \mathbb{R}$ denote the penalty parameters.

We then split (9) as two sub-problems which are expressed by

The sub-problem in (10) can be solved by soft-thresholding in a group-wise manner [38], i.e.

$$\mathbf{x}^{(k+1)} = \arg\min_{\mathbf{x}} \sum_{i=1}^{N} \left\|\mathbf{x}_{S_i}^{(k)}\right\|_2 - \boldsymbol{\gamma}_1^{\mathrm{T}}\mathbf{x}^{(k)} + \frac{\alpha_1}{2}\left\|\mathbf{x}^{(k)} - \Delta\boldsymbol{\sigma}\right\|_2^2 \tag{10}$$

$$\Delta\boldsymbol{\sigma}^{(k+1)} = \arg\min_{\Delta\boldsymbol{\sigma}} \left\{ \boldsymbol{\gamma}_1^{\mathrm{T}}\Delta\boldsymbol{\sigma}^{(k)} + \frac{\alpha_1}{2}\left\|\mathbf{x} - \Delta\boldsymbol{\sigma}^{(k)}\right\|_2^2 \\ -\boldsymbol{\gamma}_2^{\mathrm{T}}\mathbf{J}\Delta\boldsymbol{\sigma}^{(k)} + \frac{\alpha_2}{2}\left\|\mathbf{J}\Delta\boldsymbol{\sigma}^{(k)} - \Delta\mathbf{V}\right\|_2^2 \right\} \tag{11}$$

The sub-problem in (10) can be solved by soft-thresholding in a group-wise manner [38], i.e.

$$\mathbf{x}_{S_i} = \max\left\{\left\|\Delta\boldsymbol{\sigma}_{S_i} + \frac{1}{\alpha_1}(\boldsymbol{\gamma}_1)_{S_i}\right\|_2 - \frac{1}{\alpha_1}, 0\right\} \cdot \\ \frac{\Delta\boldsymbol{\sigma}_{S_i} + \frac{1}{\alpha_1}(\boldsymbol{\gamma}_1)_{S_i}}{\left\|\Delta\boldsymbol{\sigma}_{S_i} + \frac{1}{\alpha_1}(\boldsymbol{\gamma}_1)_{S_i}\right\|_2} \tag{12}$$

While the sub-problem in (11) is a convex quadratic problem, which can be solved directly by asserting its gradient to zero, i.e.

$$\boldsymbol{\gamma}_1 + \alpha_1\left(\Delta\boldsymbol{\sigma}^{(k)} - \mathbf{x}\right) + \mathbf{J}^T\left(\alpha_2\left(\mathbf{J}\Delta\boldsymbol{\sigma}^{(k)} - \Delta\mathbf{V}\right) - \boldsymbol{\gamma}_2\right) = 0 \tag{13}$$

After solving these two sub-problems, we update the multipliers:

$$\begin{cases} \boldsymbol{\gamma}_1 = \boldsymbol{\gamma}_1 - \eta_1\alpha_1(\mathbf{x} - \Delta\boldsymbol{\sigma}) \\ \boldsymbol{\gamma}_2 = \boldsymbol{\gamma}_2 - \eta_2\alpha_2(\mathbf{J}\Delta\boldsymbol{\sigma} - \Delta\mathbf{V}) \end{cases} \tag{14}$$

where $\eta_1, \eta_2 \in \mathbb{R}$ represents the step size.

In summary, the pseudo-code implementation of the DL-GS algorithm is presented in Algorithm 1.

Algorithm 1: DL-GS Algorithm

Input: Boundary voltage measurement $\Delta\mathbf{V}$.

Initialize: $\mathbf{x}$, $\Delta\boldsymbol{\sigma}$, $\boldsymbol{\gamma_1}$, $\boldsymbol{\gamma_2}$, η_1, η_2, α_1, α_2.

1 Calculate the binary mask $\mathbf{M}$ using FC-UNet;

2 Calculate the group index vector based on S;

3 **while** *the stopping criterion is not satisfied* **do**

    a) Solve the first sub-problem (10) using (12);

    b) Solve the second sub-problem (11) using (13);
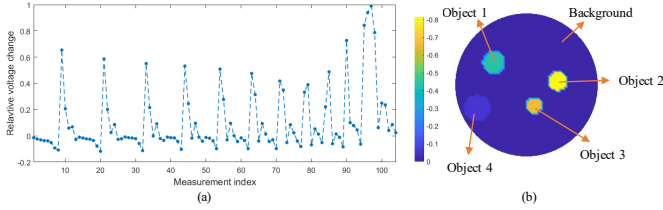
    c) Update multipliers using (14);

    end

Output: Estimated conductivity change $\Delta\boldsymbol{\sigma}$.

Fig. 4. A 4-object example of simulation data. (a) Boundary voltage change. (b) Corresponding conductivity distribution.

C. Evaluation Metrics

We quantitatively evaluate the performance of image reconstruction algorithms using Correlation Coefficient (CC), which is defined as

$$CC = \frac{\sum_{i=1}^{N}(\Delta\hat{\sigma}_i - \overline{\Delta\hat{\boldsymbol{\sigma}}})(\Delta\sigma_i - \overline{\Delta\boldsymbol{\sigma}})}{\sqrt{\sum_{i=1}^{N}(\Delta\hat{\sigma}_i - \overline{\Delta\hat{\boldsymbol{\sigma}}})^2 \sum_{i=1}^{N}(\Delta\sigma_i - \overline{\Delta\boldsymbol{\sigma}})^2}} \quad (15)$$

where $\Delta\hat{\boldsymbol{\sigma}}$ and $\Delta\boldsymbol{\sigma}$ represents the predicted conductivity and ground truth, respectively; $\Delta\hat{\sigma}_i$ and $\Delta\sigma_i$ denotes the ith element of $\Delta\hat{\boldsymbol{\sigma}}$ and $\Delta\boldsymbol{\sigma}$, respectively; $\overline{\Delta\hat{\boldsymbol{\sigma}}}$ is the mean of $\Delta\hat{\boldsymbol{\sigma}}$, and $\overline{\Delta\boldsymbol{\sigma}}$ is the mean of $\Delta\boldsymbol{\sigma}$; N is the total number of pixels. A larger CC indicates better image quality.

III. EXPERIMENTAL SETUP

A. Data Set Generation

1) Simulation Data: To generate data set for FC-UNet training, we model a circular 16-electrode EIT sensor using COMSOL Multiphysics. We adopt adjacent measurement strategy and discretize the sensing region with 3228 pixels.

3D cultivated cell aggregates are approximately circular. Therefore, we consider circular phantoms with randomly assigned object numbers (from 1 to 4), size (from 0.03d to 0.3d; d is the sensor diameter), location and conductivity values. The conductivity of the circular objects is bounded within the range of 0.0001 $S \cdot m^{-1}$ and 0.05 $S \cdot m^{-1}$. The background substance has a constant conductivity of 0.05 $S \cdot m^{-1}$. Forward problem of EIT is calculated regarding each randomly generated phantom to obtain the corresponding measurement. An example of the generated phantom with its voltage data is shown in Fig. 4.

We finally generated 29,333 multi-level EIT samples, including 7035 1-object samples, 7298 2-object samples, 7500 3-object samples and 7500 4-object samples. We then divided

Data set	Training	Validation	Testing
Noise Free Samples	24,000	2,000	3,333
50dB Samples	12,000	1,000	3,333
40dB Samples	12,000	1,000	3,333
30dB Samples	/	/	3,333
Total Samples	**48,000**	**4,000**	**13,332**

this data set into training set (6000 samples from each case), validation set (500 samples from each case), and testing set (the remaining samples). The three subsets contain 24k, 2k and 3,333 samples, respectively.

In addition, we implement data augmentation by adding noise to measurement data in both training and validation sets, in order to enhance the robustness of our model when system noise or error is encountered. Additive noise with the Signal-to-Noise Ratio (SNR) of 50dB is added to half of the training and validation samples for each case. Additive noise with the SNR of 40dB is then added to the other half of the training and validation data. As a result, both training and validation data are doubled. Testing data are added noise with SNR of 50dB, 40dB and 30dB. Table I summarizes the constitution of the training, validation, and testing data sets.

2) Experimental Data: To validate the multi-level performance of the proposed method using mEIT, we employed the 16-electrode miniature EIT sensor designed in [39] to collect phantom experiment data (see Fig. 5). The inner diameter of the sensing chamber is 15 mm and the height is 10 mm. A carrot and a rubber cylinder, which has similar size but different conductivity (rubber: non-conductive; carrot: less conductive than background), were imaged. Additionally, we conducted experiments on MCF-7 human breast cancer cell aggregates to examine the performance in cell imaging. In this case, a 16-electrode quasi-2D miniature EIT sensor [40], which is able to incorporate impedance sensing with optical imaging modalities, and a multi-frequency EIT system designed by the authors [41] were employed for cell imaging (MCF-7 cell: less conductive than background). The schematic and manufactured miniature EIT sensor, and 3D cultivated MCF-7 cell aggregates are presented in Fig. 6. The sensing chamber has a diameter of 14mm and a height of 1.6mm. Two MCF-7 human breast cancer cell aggregates with a diameter of approximately 2mm were imaged. More details regarding experimental phantoms are presented in Section IV-C.

B. Data Normalization

In FC-UNet training, to reduce the effect of sensor imperfection, we normalize the voltage measurement and conductivity distribution by

$$\Delta\mathbf{V}_n = \frac{\mathbf{V}_{mea} - \mathbf{V}_{ref}}{\mathbf{V}_{ref}} \quad (16)$$

$$\Delta\boldsymbol{\sigma}_n = \frac{\boldsymbol{\sigma}_{mea} - \boldsymbol{\sigma}_{ref}}{\boldsymbol{\sigma}_{ref}} \quad (17)$$

where $\mathbf{V}_{ref}$ and $\boldsymbol{\sigma}_{ref}$ represent respectively the measurement and conductivity distribution when the sensing region is only
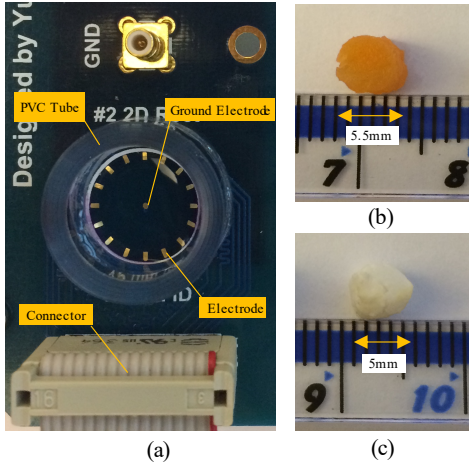
Fig. 5. Experimental setup for carrot and rubber phantom. (a) The miniature EIT sensor [39]. (b) Carrot cylinder. (c) Rubber cylinder.

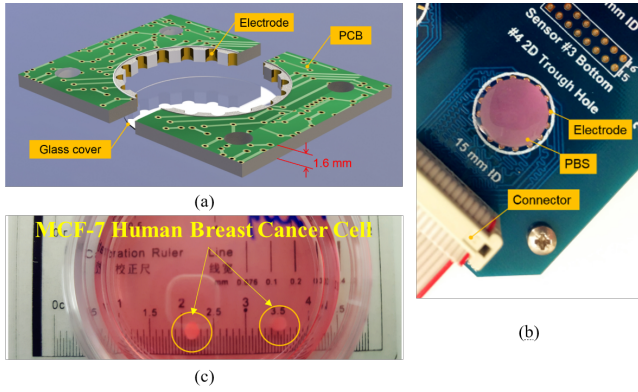Fig. 7. The learning curves of the FC-UNet.

Fig. 6. Experimental setup for cell imaging. (a) Sensor schematic. (b) The manufactured quasi-2D miniature EIT sensor [40]. (c) MCF-7 cell aggregates.

filled with background substance; $\mathbf{V}_{mea}$ and $\boldsymbol{\sigma}_{mea}$ denote respectively the measurement and conductivity distribution after objects are present in the sensing region.

During training, one option is to retain the varying conductivity changes from (17), in which case the FC-UNet solves a regression problem. Then all non-zero pixels of the output are then set as one to generate the binary mask. Whilst the alternative is to binarize the conductivity values from (17) before training, and use this binary format as ground truth so that it becomes a classification task. We investigated both options and found out that in terms of accuracy, the latter performs better. Therefore, we adopt the latter in training.

C. Network Training

To train the FC-UNet model, we use the well-known Adam [42] for optimization. The initial learning rate is 0.0001. We also introduce the step decay for the training, where the learning rate is reduced by a factor of 0.1 every 25 epochs to promote faster convergence and higher accuracy. The effect of step decay will be discussed in Section IV-A. The model is trained with a batch size of 25.

Inspired by transfer learning which takes a pre-trained model of one task as a starting point for another task [43],
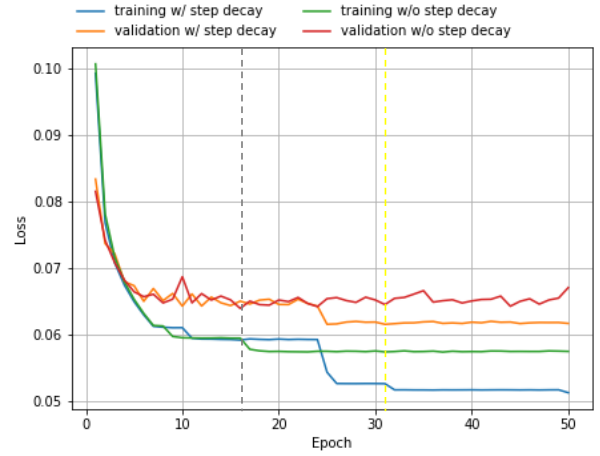
we initialize weights for the fully connected layer with the pre-calculated least-squares (LS) solution of (2) using training data, instead of random weights. During training, these weights are further fine-tuned. The rest is initialized with random weights as usual.

The maximum number of training epochs is set as 50. The final model is selected according to the validation loss. That is, the training process stops at the point with the least validation loss. Experiments are implemented using NVIDIA P5000 GPUs.

IV. RESULTS AND DISCUSSIONS

A. Learning Curve of FC-UNet

Learning curves (see Fig. 7) illustrate the effect of step decay when training the FC-UNet. It can be observed that the training curve in blue using step decay shows a steep decrease at the 25th epoch when the learning rate is reduced by a factor of 0.1. This curve has lower asymptote at the end compared to the training curve in green, which utilizes a constant learning rate in the entire learning process and converges at a local minimum. This implies that introducing the step decay term can promote convergence at a better minimum and achieve considerable lower loss.

The orange and red lines represent the validation loss curves with and without step decay, respectively. In initial phase, both validation losses are smaller than the corresponding training losses. This means more training is required since the model underfits the training data. After 3 epochs, the training loss starts exceeding the validation loss. The dashed line in grey and the one in yellow indicate where the lowest validation loss is reached and the training process stops. Obviously, the step decay contributes to much better validation performance.

B. Results Based on Simulation Data

Fig. 8(a) shows four multi-level conductivity phantoms in testing data set. In simulation, additive Gaussian noise with SNR of 50dB was added to measurements. Theoretically, as the number of inclusion and conductivity level increases,
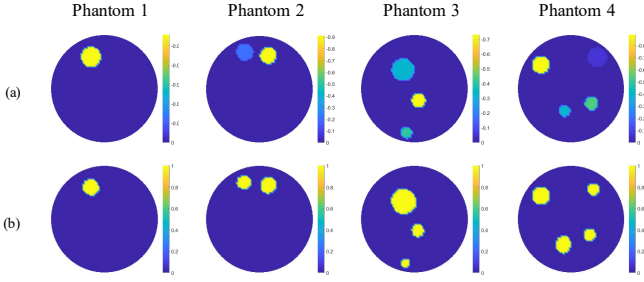
Fig. 8. Multi-level conductivity phantoms and binary masks generated by FC-UNet. (a) Ground Truth (b) Corresponding binary masks from FC-UNet.
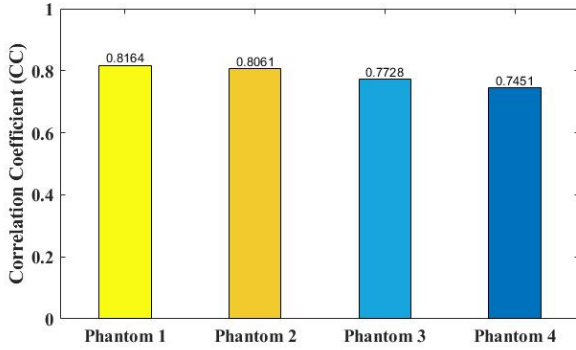

Fig. 9. Correlation coefficients of the FC-UNet results.

TABLE II
COMPARISON OF AVERAGE CC

Image Reconstruction	SNR			
Algorithm	Noise Free	50dB	40dB	30dB
l_1 [17]	0.5268	0.5276	0.5244	0.5253
SBL [19]	0.5634	0.5633	0.5628	0.5617
AGS [18]	0.5263	0.5224	0.5196	0.4982
LeNet [27]	0.6445	0.6420	0.6124	0.5233
DL-GS	**0.7215**	**0.6639**	**0.6161**	**0.5648**

TABLE III
COMPARISON OF AVERAGE MODEL EXECUTION TIME PER IMAGE [S]

Image Reconstruction	SNR			
Algorithm	Noise Free	50dB	40dB	30dB
l_1 [17]	0.4867	0.4878	0.4636	0.4689
SBL [19]	12.95	13.00	13.03	12.85
AGS [18]	0.7388	0.7573	0.7520	0.7396
LeNet [27]	**0.22e-3**	**0.26e-3**	**0.25e-3**	**0.27e-3**
DL-GS	**0.1114**	**0.1131**	**0.1128**	**0.1127**

estimation of conductivity distribution in the binary form is more challenging. Fig. 8(b) gives binary results generated by FC-UNet and correlation coefficients of all phantoms are shown in Fig. 9. The numerical results suggest that FC-UNet performs well on predicting the positions and shapes of the given multi-level conductivity phantoms.

We then compare the multi-level reconstruction results of the proposed DL-GS method with some state-of-the-art EIT image reconstruction algorithms, i.e. l_1 regularization (l_1) [17], Sparse Bayesian Learning (SBL) [19], Adaptive Group Sparsity (AGS) [18], and LeNet [27]. During implementation, stopping tolerance is set as $1e - 7$. The maximum iteration numbers of l_1, SBL, AGS, and DL-GS are respectively set as 50, 20, 500, and 500. The block size of SBL is 4. For AGS, the maximum diameter of the group is set as 10 pixels. The penalty vectors of AGS and DL-GS are respectively $[1/\overline{|\Delta \mathbf{V}|}, 5/\overline{|\Delta \mathbf{V}|}]$, and $[10/\overline{|\Delta \mathbf{V}|}, 0.1/\overline{|\Delta \mathbf{V}|}]$ throughout the experiment. Training procedure for LeNet is the same as that for FC-UNet except that mean square error is the loss function.

Fig. 10 shows the relative conductivity changes reconstructed by different algorithms. For the phantom with a small conductivity change in the first row, AGS recovers better size compared to l_1, SBL, and LeNet whereas they all underestimate the object dimension. In contrast, DL-GS provides much better results in terms of both structure and conductivity variation. As the number of object and conductivity level increases (see phantoms from the second to the fourth row), l_1, SBL, AGS, and LeNet fail to reconstruct the shape and conductivity difference, and objects with smaller

conductivity changes are barely recovered. In comparison, DL-GS outputs more accurate shapes as well as conductivity variations. Particularly, when there are four objects, DL-GS is the only algorithm that manages to recognize them all and recovers more faithful conductivity information.

Table II compares the average CC of all phantoms in the testing set when noise of various levels is added to measurements. We can observe that DL-GS outperforms the other algorithms in all cases, with the highest CC. Noting that it performs even better than the purely deep learning method LeNet by 5.9%. All algorithms exhibit their robustness to noise and there is a continuous decrease in CC with the growth of SNR. Table III reports the average model execution time per image. LeNet achieves the fastest running time, indicating the prominent advantage of using deep neural network. DL-GS is the second fastest algorithm, substantially 6.5 times better than AGS on average. As expected, the FC-UNet significantly reduces the computation time for pixel grouping whereas in AGS, the initial grouping from one-step Gaussian Newton requires much longer time.

C. Results Based on Experimental Data

In addition to validation with simulation data, we collect experimental data using different miniature EIT sensors to examine the performance of DL-GS. When implementing l_1, SBL, AGS, LeNet, and DL-GS, all parameters are the same as in simulation settings.

Three phantoms as shown in the first column of Fig. 11 were imaged. The first phantom contains carrot and rubber cylinders with saline as the background. The excitation frequency is 20kHz and the maximum iteration of DL-GS is 350. Intrinsically, rubber at the lower left corner has lower conductivity than carrot (i.e. rubber leads to larger conductivity change with respect to background), which is successfully recovered by all algorithms but most significantly by LeNet and DL-GS. DL-GS also reconstructs the best shape of both objects with clear boundary. The other two phantoms image two cell aggregates. Observing the results, l_1 can roughly
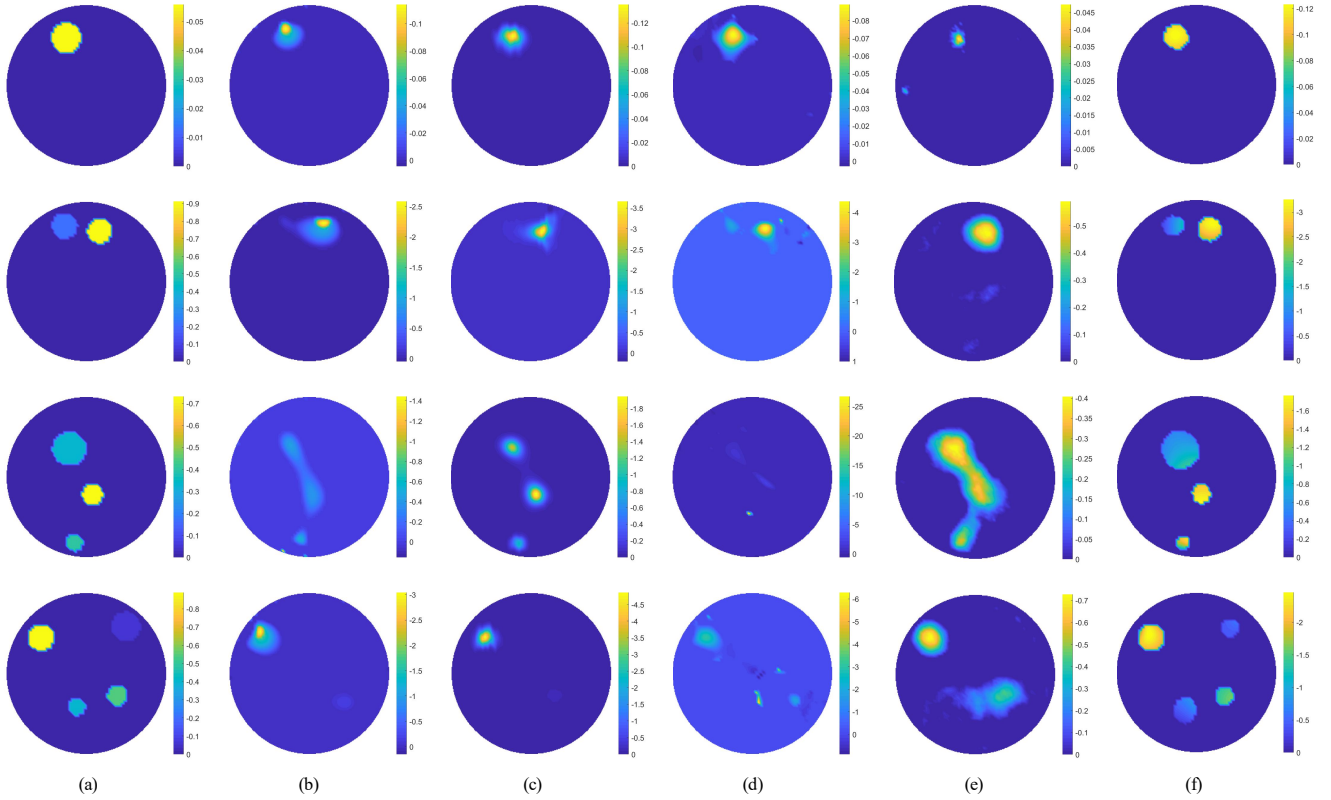
Fig. 10. Image reconstruction results of four phantoms from testing data set (SNR = 50 dB) (note we use inverted color bar). (a) Ground truth (b)-(e) Corresponding results of l_1, SBL, AGS, LeNet, and DL-GS respectively.

identify both cell aggregates but there exists obvious distortion and artifacts. SBL consistently manages to reconstruct the two cell aggregates with good positions, whilst it underestimates the size of the cell and the artifact at the center of ROI is also distinct. AGS fails to reconstruct the phantoms clearly, which is even worse than l_1 and SBL. The underlying reason might be that AGS utilizes one-step algorithm to estimate the structural information, but in this case the one-step algorithm struggles to provide meaningful results for pixel grouping. LeNet performs well when the two cell aggregates are far from each other but has the same issues as l_1 when they become closer. With regard to DL-GS, it is able to obtain much better shape and position of each cell aggregate for both cases. Compared to l_1, SBL, and AGS, DL-GS yields sharper edges for all reconstructed cell aggregates. Table IV gives CC of experimental results, further confirming the successful transition of DL-GS to various experimental data. DL-GS achieves the highest CC for all the phantoms, outperforming the other algorithms. The results indicate that DL-GS can be generalized to the mEIT setup and facilitate robust and high-quality cell imaging.

V. CONCLUSIONS

In this paper, we proposed a deep learning and group sparsity regularization based hybrid algorithm for 3D cultivated cell imaging with miniature EIT sensors. This work specifically focused on the challenge of performing multi-level

TABLE IV
CC OF EXPERIMENTAL RESULTS

Phantom	l_1 [17]	SBL [19]	AGS [18]	LeNet [27]	DL-GS
1	0.4809	0.4473	0.3188	0.5449	**0.7477**
2	0.6490	0.6271	0.3666	0.7704	**0.8008**
3	0.7145	0.6689	-0.0020	0.7224	**0.7650**

conductivity imaging under multiple objects' setup. We established a novel EIT data set with continuously varying conductivity values for different sensing objects. A FC-UNet model was then developed to provide structural information of multilevel conductivity distribution. Afterwards, we integrated this structural information into group sparsity regularization to estimate the continuous conductivity values. Both simulation and experiments demonstrated that the proposed DL-GS method outperforms the other given image reconstruction approaches and demonstrates strong generalization ability on a practical miniature EIT sensor to image MCF-7 cell aggregates. Whilst the proposed approach is limited to 2D reconstruction in this work, it could be readily extended to 3D imaging. In the future, we will investigate the 3D hybrid learning framework with 3D miniature EIT setups.

REFERENCES

[1] B. A. Justice, N. A. Badr, and R. A. Felder, "3D cell culture opens new dimensions in cell-based assays," *Drug Discov. today*, vol. 14, no. 1–2, pp. 102–107, Jan. 2009.
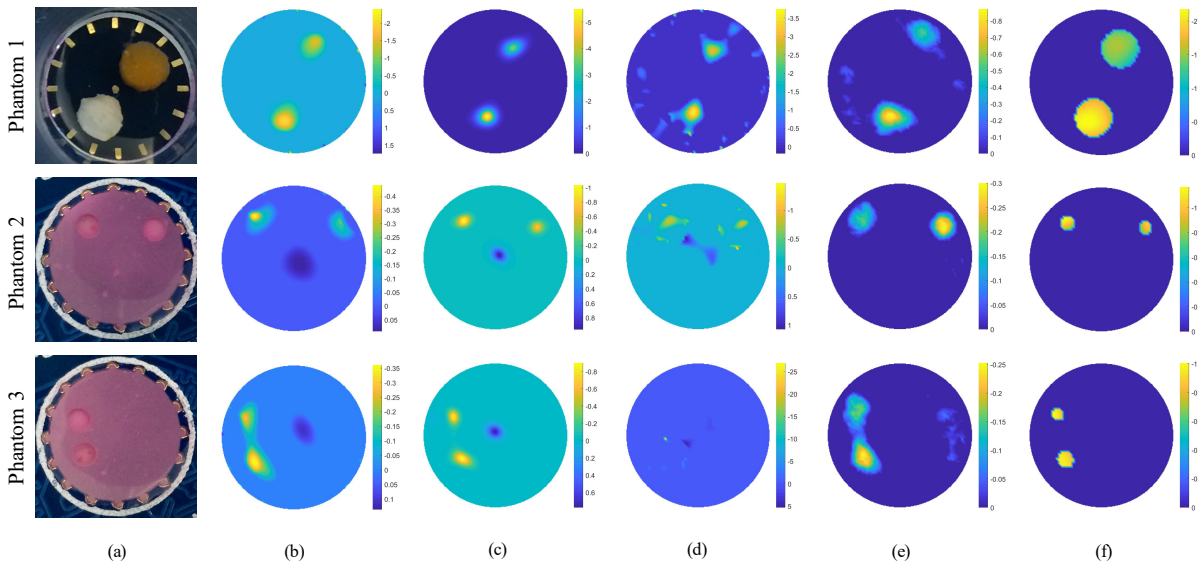
Fig. 11. Image reconstruction results using experimental data (note we use inverted color bar). (a) Three setups. (b)-(e) corresponds to results of l_1, SBL, AGS, LeNet, and DL-GS, respectively.

[2] R. H. Bayford, "Bioimpedance tomography (electrical impedance tomography)," *Annu. Rev. Biomed. Eng.*, vol. 8, pp. 63–91, Aug. 2006.

[3] B. Schullcke, B. Gong, S. Krueger-Ziolek, M. Soleimani, U. Mueller-Lisse, and K. Moeller, "Structural-functional lung imaging using a combined CT-EIT and a Discrete Cosine Transformation reconstruction method," *Sci. Rep.*, vol. 6, pp. 25951, May. 2016.

[4] M. H. Choi, T. J. Kao, D. Isaacson, G. J. Saulnier, and J. C. Newell, "A reconstruction algorithm for breast cancer imaging with electrical impedance tomography in mammography geometry," *IEEE Trans. Biomed. Eng.*, vol. 54, no. 4, pp. 700—710, Apr. 2007.

[5] R. J. Sadleir, S. Z. Sajib, H. J. Kim, O. I. Kwon, and E. J. Woo, "Simulations and phantom evaluations of magnetic resonance electrical impedance tomography (MREIT) for breast cancer detection." *J. Magn. Reson.*, vol. 230, pp. 40—49, May. 2013.

[6] A. Romsauerova, A. McEwan, L. Horesh, R. Yerworth, R. H. Bayford, and D. S. Holder, "Multi-frequency electrical impedance tomography (EIT) of the adult human head: initial findings in brain tumours, arteriovenous malformations and chronic stroke, development of an analysis method and calibration." *Physiol. Meas.*, vol. 27, no. 5, pp. S147—61, Apr. 2006.

[7] N. Goren, J. Avery, T. Dowrick, E. Mackle, A. Witkowska-Wrobel, D. Werring, and D. Holder, "Multi-frequency electrical impedance tomography and neuroimaging data in stroke patients," *Sci. Data*, vol. 5, Jul. 2018, Art. no. 180112.

[8] Y. Yang, J. Jia, S. Smith, N. Jamil, W. Gamal, and P. O. Bagnaninchi, "A miniature electrical impedance tomography sensor and 3-D image reconstruction for cell imaging," *IEEE Sensors J.*, vol. 17, no. 2, pp. 514—523, Jan. 2017.

[9] Y. Yang, H. Wu, J. Jia, P. O. Bagnaninchi, "Scaffold-based 3-D Cell Culture Imaging Using a Miniature Electrical Impedance Tomography Sensor." *IEEE Sensors J.*, vol. 19, no. 20, pp. 9071—9080, Jun. 2019.

[10] H. Wu, Y. Yang, P. O. Bagnaninchi, and J. Jia, "Electrical impedance tomography for real-time and label-free cellular viability assays of 3D tumour spheroids," *Analyst.*, vol. 143, no. 17, pp. 4189–4198, 2018. DOI: 10.1039/C8AN00729B.

[11] H. Wu, W. Zhou, Y. Yang, J. Jia, and P. Bagnaninchi, "Exploring the potential of electrical impedance tomography for tissue engineering applications," *J. Mater. Sci.,* vol. 11, no. 6, pp. 930, 2018.

[12] X. Li, F. Yang, W. He, and B. Rubinsky, "A theoretical study on real time monitoring of single cell mitosis with micro electrical impedance tomography," *Biomed. Microdevices,* vol. 21, no. 4, pp. 102, 2019.

[13] R. V. Davalos, D. M. Otten, L. M. Mir, and B. Rubinsky, "Electrical impedance tomography for imaging tissue electroporation," *IEEE. Trans. Biomed. Eng.,* vol. 51, no. 5, pp.761-767, 2004.

[14] M. Lukaschewitsch, P. Maass, and M. Pidcock, "Tikhonov regularization for electrical impedance tomography on unbounded domains," *Inverse Problems*, vol. 19, no. 3, p. 585, 2003.

[15] A. Borsic, B. M. Graham, A. Adler, and W. Lionheart, "In vivo impedance imaging with total variation regularization," *IEEE Trans. Med. Imag.*, vol. 29, no. 1, pp. 44–54, Jan. 2010.

[16] B. Jin, T. Khan, and P. Maass, "A reconstruction algorithm for electrical impedance tomography based on sparsity regularization," *Int. J. Numer. Methods Eng.*, vol. 89, no. 3, pp. 337–353, 2012.

[17] J. N. Tehrani, A. McEwan, C. Jin, and A. van Schaik, "L1 regularization method in electrical impedance tomography by using the L1-curve (Pareto frontier curve)," *Appl. Math. Model.*, vol. 36, no. 3, pp. 1095–1105, Mar. 2012.

[18] Y. Yang and J. Jia, "An image reconstruction algorithm for electrical impedance tomography using adaptive group sparsity constraint," *IEEE Trans. Instrum. Meas.*, vol. 66, no. 9, pp. 2295–2305, Sep. 2017.

[19] S. Liu, J. Jia, Y. D. Zhang, and Y. Yang, "Image reconstruction in electrical impedance tomography based on structure-aware sparse Bayesian learning," *IEEE Trans. Med. Imag.*, vol. 37, no. 9, pp. 2090–2102, Sep. 2018.

[20] S. Liu, H. Wu, Y. Huang, Y. Yang, and J. Jia, "Accelerated structure-aware sparse Bayesian learning for three-dimensional electrical impedance tomography," *IEEE Trans. Ind. Inf.*, vol. 15, no. 9, pp. 5033–5041, Sept. 2019.

[21] G. Wang, J. C. Ye, K. Mueller, and J. A. Fessler, "Image reconstruction is a new frontier of machine learning," *IEEE Trans. Med. Imag.*, vol. 37, no. 6, pp. 1289–1296, Jun. 2018.

[22] Y. Han and J. C. Ye, "Framing U-Net via deep convolutional framelets: Application to sparse-view CT," *IEEE Trans. Med. Imag.*, 2018, DOI:10.1109/TMI.2018.2823768.

[23] B. Zhu, J. Z. Liu, S. F. Cauley, B. R. Rosen, and M. S. Rosen, "Image reconstruction by domain-transform manifold learning," *Nature*, vol. 555, no. 7697, pp. 487–492, 2018.

[24] H. K. Aggarwal, M. P. Mani, and M. Jacob, "MoDL: Model-based deep learning architecture for inverse problems," *IEEE Trans. Med. Imag.*, vol. 38, no. 2, pp. 394–405, Feb. 2019.

[25] D. Wu, K. Kim, B. Dong, and Q. Li. (2017). "End-to-end abnormality detection in medical imaging." [Online]. Available: https://arxiv.org/abs/1711.02074

[26] J. Zheng and L. Peng, "An autoencoder-based image reconstruction for electrical capacitance tomography," *IEEE Sensors J.*, vol. 18, no. 13, pp. 5464–5474, Jul. 2018.

[27] C. Tan, S. H. Lv, F. Dong, and M. Takei, "Image reconstruction based on convolutional neural network for electrical resistance tomography," *IEEE Sensors J.*, vol. 19, no. 1, pp. 196–204, Jan. 2019.

[28] D. Hu, K. Lu, and Y. Yang, "Image reconstruction for electrical impedance tomography based on spatial invariant feature maps and convolutional neural network," in *Proc. IEEE Int. Conf. Imag. Syst. Techn.,*, AUH, United Arab Emirates, Dec. 2019, pp. 1–6.

[29] S. J. Hamilton and A. Hauptmann, "Deep D-bar: Real-time electrical impedance tomography imaging with deep neural networks," *IEEE Trans. Med. Imag.,* vol. 37, no. 10, pp. 2367–2377, Oct. 2018.

[30] Z. Wei, D. Liu, and X. Chen, "Dominant-current deep learning scheme for electrical impedance tomography," *IEEE Trans. Biomed. Eng.,* vol. 66, no. 9, pp. 2546–2555, Sep. 2019.

[31] K. S. Cheng et al., "Electrode models for electric current computed tomography," *IEEE Trans. Biomed. Eng.*, vol. 36, no. 9, pp. 918–924, 1989.

[32] O. Ronneberger, P. Fischer, and T. Brox, "U-net: Convolutional networks for biomedical image segmentation," in *Proc. Med. Image Comput. Comput.-Assisted Intervention*, 2015, pp. 234–241.

[33] Y. Yang, J. Jia, N. Polydorides, and H. McCann, "Effect of structured packing on EIT image reconstruction," in *Proc. Proc. IEEE Int. Conf. Imag. Syst. Techn.*, Santorini, Greece, Oct. 2014, pp. 53–58.

[34] J. Huang and T. Zhang, "The benefit of group sparsity," *Ann. Statist.,* vol. 38, no. 4, pp. 1978–2004, 2010.

[35] G. Obozinski, B. Taskar, and M. Jordan, "Joint covariate selection and joint subspace selection for multiple classification problems," *J. Stat. Comput.,* vol. 20, no. 2, pp. 231–252, 2009.

[36] M. Fukushima, "Application of the alternating direction method of multipliers to separable convex programming problems," *Comput. Optim. Appl.,* vol. 1, no. 1, pp. 93–111, Oct. 1992.

[37] J. Wang, J. Huang, F. Zhang, and W. Wang, "Group sparse recovery in impulsive noise via alternating direction method of multipliers," *Appl. Comput. Harmon. Anal.,* vol. 49, no. 3, pp. 831-862, 2020.

[38] W. Deng, W. Yin, and Y. Zhang, "Group sparse optimization by alternating direction method," in *Proc. SPIE*, Wavelets Sparsity XV, vol. 8858. Sep. 2013, pp. 88580R, DOI: 10.1117/12.2024410.

[39] Y. Yang, J. Jia, S. Smith, N. Jamil, W. Gamal and P. Bagnaninchi, "A Miniature Electrical Impedance Tomography Sensor and 3-D Image Reconstruction for Cell Imaging," *IEEE Sensors Journal*, vol. 17, no. 2, pp. 514-523, 15 Jan.15, 2017, doi: 10.1109/JSEN.2016.2631263.

[40] Y. Yang, H. Wu, and J. Jia, "Quasi-2D EIT-optical Dual Modality Sensor for Cellular Imaging," ELECTRICAL IMPEDANCE TOMOGRAPHY., 2018.

[41] Y. Yang and J. Jia, "A multi-frequency electrical impedance tomography system for real-time 2D and 3D imaging," *Rev. Sci. Instrum.*, vol. 88, no. 8, p. 085110, 2017.

[42] D. P. Kingma and J. L. Ba, "Adam: A method for stochastic optimization," in *Proc. Int. Conf. Learn. Represent.*, 2015, pp. 1–41.

[43] L. Torrey and J. Shavlik, "Transfer learning," in *Handbook of Research on Machine Learning Applications and Trends: Algorithms, Methods, and Techniques,* Hershey, PA, USA: IGI Global, 2009.